

Full-field mapping of spatially varying polarization entanglement generated from spontaneous parametric down-conversion

Cheng Li,^{1,*} Girish Kulkarni,^{1,2} Isaac Soward,¹ Yingwen Zhang,^{1,3} Jeremy Upham,¹
Duncan England,³ Andrei Nomerotski,^{4,5} Ebrahim Karimi,^{1,3,6} and Robert Boyd^{1,7,†}

¹*Department of Physics, University of Ottawa, Ottawa, ON K1N 6N5, Canada*

²*Department of Physics, Indian Institute of Technology Ropar, Rupnagar, Punjab 140001, India.*

³*National Research Council, Ottawa, ON K1A 0R6, Canada*

⁴*Faculty of Nuclear Sciences and Physical Engineering,
Czech Technical University, Prague 115 19, Czech Republic*

⁵*Department of Electrical and Computer Engineering,
Florida International University, Miami, FL 33174, USA*

⁶*Institute for Quantum Studies, Chapman University, Orange, CA 92866, USA*

⁷*Institute of Optics, University of Rochester, Rochester, NY 14627, USA*

Two-photon states generated from spontaneous parametric down-conversion (SPDC) can display entanglement in all degrees of freedom (DoFs) of light, including spatial, temporal, and polarization. The coupling between different DoFs of a two-photon state has been shown to display rich structures that enable novel and robust information processing schemes. While existing literature has studied these couplings by post-selecting the SPDC field, a comprehensive understanding of the inherent spatial-polarization coupling produced in the SPDC process is still lacking. This work produces a full spatial map of the polarization entanglement generated across the entire SPDC field. We observe an entire class of near-maximally polarization-entangled states with an average concurrence of 0.8303 ± 0.0004 , which, together with a certified spatial dimensionality of 148, could potentially offer access to a 251-dimensional hyperentanglement. The spatial-polarization coupling manifests as radially or linearly varying polarization-entangled states, whose wavefunctions are dependent on the transverse momenta of the down-converted photons and the pump beam, respectively. Our study lays important groundwork for further exploiting the coupling between entanglement in different DoFs for future quantum technologies.

I. INTRODUCTION

Spontaneous parametric down-conversion (SPDC) has been a major workhorse for generating entangled two-photon states [1–3], enabling numerous applications in quantum information processing. In SPDC, a photon from a pump beam, which has a higher optical frequency, interacts with a second-order nonlinear medium to be annihilated and produce a pair of down-converted photons with lower frequencies [2]. The down-converted photons, which are commonly referred to as signal and idler, can exhibit entanglement in all degrees of freedom (DoFs) of light, including spatial, temporal, and polarization.

Studying the coupling between different DoFs is a crucial step towards a comprehensive understanding of SPDC-based entanglement generation and engineering novel entangled photon states for practical applications [4, 5]. An important aspect of this subject is the coupling between spatial and polarization DoFs in SPDC. Such cross-DoF couplings can be exploited to enable novel and efficient quantum information applications. For instance, it was shown that quantum correlations across spatial and polarization DoFs can enable novel and more robust information encoding schemes and demonstrate

topological resilience against environmental noise [6]. Moreover, the spatially varying polarization correlations in a photonic entangled state can also be harnessed to enable quantum holographic imaging [7] or engineer photonic cluster states for efficient quantum computation [8, 9]. From a fundamental perspective, studies have shown that spatial modes of the pump beam can influence the polarization entanglement of the down-converted photons [10, 11], indicating the opportunity of directly engineering the couplings between different DoFs in a photonic entangled state, or encoding phase images in the two-photon correlations [12] by shaping the pump beam.

The spatial-polarization coupling in SPDC commonly manifests as two-photon states with spatially varying polarization entanglement. Although one can readily produce these features from SPDC using a paired crystal configuration [13, 14], the large spatial dimensionality of the SPDC field hinders the efficient characterization of them. For instance, a full state tomography for a bipartite state with local dimensionality d in a single DoF requires $\mathcal{O}(d^4)$ single-outcome projective measurements [15–17]. Since the total dimensionality of a quantum state scales with the product of dimensionality in each constituent DoF, the need to address correlations, both within and between different DoFs, only adds to the complexity of the problem. Without comprehensively resolving the polarization entanglement produced in each spatial mode, the rich structures resulting from the

* cli221@uottawa.ca

† rboyd@uottawa.ca

coupling between different DoFs reduce to a mixture of distinguishable states. As a result, the full potential of SPDC-induced spatial-polarization coupling becomes inaccessible, limiting its application in practical quantum devices. For instance, a recent work indicates that even though each spatial mode in a multimode pump beam can generate maximum polarization entanglement through SPDC, detecting the two-photon states without resolving individual spatial modes can make the entanglement appear deteriorated [10].

Over the past decade, several studies have employed Tpx3Cam, a data-driven camera capable of time-stamping single photons [18–20], to enable rapid characterization of photonic entangled states produced from SPDC [21–23]. However, these works have not fully explored the coupling between different DoFs. Specifically, Ref. [21, 22] have focused only on the polarization DoF or the spatial DoF, respectively, while their photon pair sources are capable of producing spatially varying polarization-entangled states. As a result, the potential of the embedded spatial-polarization coupling has not been addressed. Furthermore, the entangled states produced in Ref. [21, 23] are first spatially postselected using single-mode fibers or polarization-maintaining fibers before being imaged onto the Tpx3Cam, and any spatial structures in the resulting polarization are imprinted by external modulation devices. Doing so effectively reduces the spatial dimensionality and obscures any spatial-polarization coupling imposed by the generation process.

In this work, we employ Tpx3Cam to comprehensively characterize the spatially varying polarization entanglement that is natively produced from SPDC. In contrast to earlier works, we image the full spatial field of SPDC without any post-processing on the resulting two-photon states. By performing spatially-resolved polarization state tomography, we confirm the generation of near-maximally polarization-entangled states across the entire spatial profile of the SPDC field, with an average concurrence of 0.8303 ± 0.0004 . Importantly, we present a complete spatial map of the polarization state generated from SPDC, revealing how polarization entanglement depends on the transverse momenta of the down-converted photons throughout the entire spatial profile of the SPDC field. Moreover, using a weakly focused pump beam, we experimentally characterize the dependence of polarization entanglement on the

angular spectrum of the pump beam. Additionally, we have estimated a maximum attainable dimensionality of spatial entanglement to be 148, which, combined with the effective dimensionality in the polarization DoF, indicates a total attainable dimensionality of 251. Our results advance the fundamental understanding of the interplay between different DoFs of a photonic entangled state, paving the way for novel applications in photonic quantum information processing.

II. EXPERIMENTAL SETUP

Fig. 1(a) depicts our experimental setup. An ultraviolet continuous-wave laser emits the pump beam with a center wavelength of 405 nm, a bandwidth of 2 nm, and a power of 20 mW. The pump beam is made polarized at 45° using a polarizing beam splitter (PBS) and a half-wave plate (HWP). A 5-mm temporal compensator (TC) quartz crystal introduces a time delay between the horizontal (H-) and vertical (V-) components of the pump beam, which pre-compensates for the temporal walk-off that the two orthogonal polarization components are expected to subsequently gather inside the BBO double-crystal [24]. The BBO crystals are each 0.5-mm-thick and identically cut for type-I phase-matching, with their optical axes oriented perpendicularly to one another [13]. A 45° -polarized photon from the pump beam can then be down-converted in either crystal with equal probability to produce a pair of H-polarized or V-polarized photons. In the experiment, we orient the double-crystal for near-collinear phase matching. The down-converted photons are separated from the pump beam using a dichroic mirror (DM), and then probabilistically split into two arms using a non-polarizing beam splitter (BS). We ignore the cases wherein both the down-converted photons exit the same port of the BS, and denote photons that are reflected as *signal* and those that are transmitted as *idler*. This beam-splitting scheme ensures that measuring the correlation between the signal arm and the idler arm resolves the full spatial profile of the SPDC. Although the probabilistic splitting reduces the coincidence rates by 50%, it does not affect the quality of entanglement or the measured spatial-polarization structure compared to those obtained with deterministic splitting, as can be seen later in Fig. 2 and Fig. 4. In the low-gain regime, the output state $|\Psi\rangle$ in the far-field can be written in the joint spatial-polarization basis as

$$|\Psi\rangle = \frac{1}{\sqrt{2}} \sum_{\mathbf{p}_s, \mathbf{p}_i} c_{\mathbf{p}_s, \mathbf{p}_i} \left[|H, \mathbf{p}_s, H, \mathbf{p}_i\rangle + e^{i\phi(\mathbf{p}_s, \mathbf{p}_i)} |V, \mathbf{p}_s, V, \mathbf{p}_i\rangle \right], \quad (1)$$

where $\mathbf{p}_{s(i)}$ represents the transverse momentum of the signal (idler) photon and $c_{\mathbf{p}_s, \mathbf{p}_i}$ are complex coefficients. The quantity $\phi(\mathbf{p}_s, \mathbf{p}_i)$ represents a phase difference

between the orthogonal polarization components of the state, which is dependent on the transverse momentum of the signal and the idler photons [25]. In what follows,

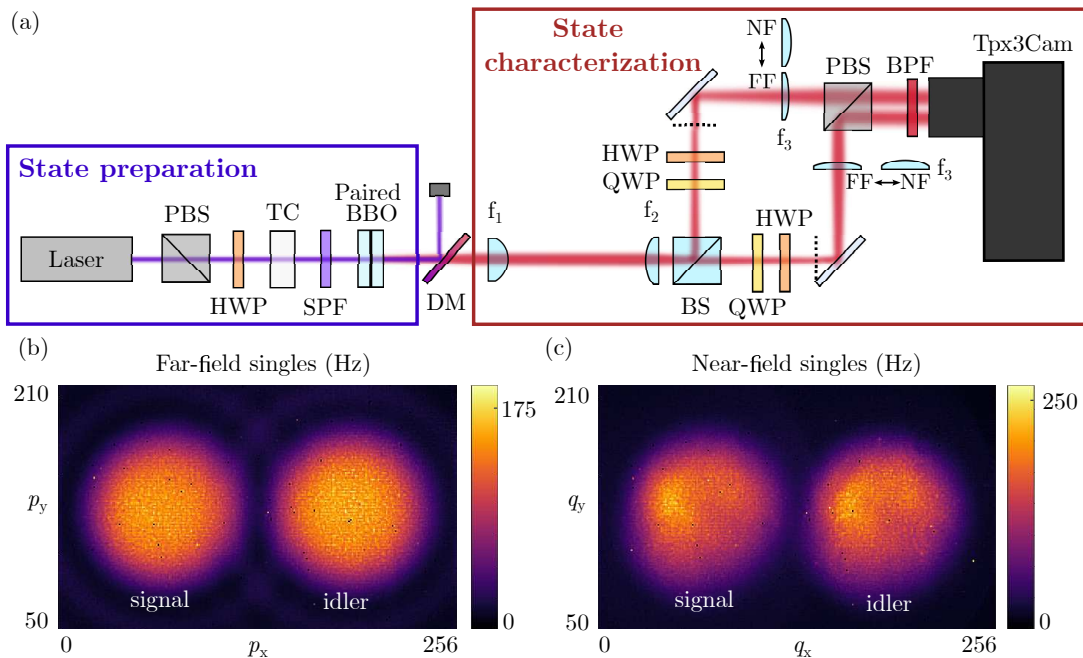


FIG. 1. (a) Schematic of the experimental setup. The β -barium borate (BBO) double-crystal produces a two-photon state, which exhibits spatially varying polarization entanglement. The Tpx3Cam captures the two-photon field in the momentum or position basis through different lens configurations and in different polarization bases through combinations of the quarter-wave plate (QWP), half-wave plate (HWP), and polarizing beam splitter (PBS). TC: temporal compensator, SPF: short-pass filter with cutoff wavelength at 500 nm, DM: dichroic mirror, BS: beam splitter, BPF: band-pass filter centered at 800 nm with a bandwidth of 40 nm. $f_1 = 50$ mm, $f_2 = 100$ mm. $f_3 = 150$ mm for far-field measurements or 75 mm for near-field measurements. Dashed lines represent the intermediate planes imaging the near-field of the crystal using f_1 and f_2 . (b-c) Time-stamp histogram of photons detected in the far-field and near-field of the crystal, representing projection onto the momentum (p) and position (q) bases of the two-photon state.

we refer to ϕ as the *two-photon polarization phase*.

The signal and idler photons then propagate through a quarter-wave plate (QWP) and a HWP before they are either transmitted or reflected by a PBS. The photons finally pass through a bandpass filter with a center wavelength of 800 nm and full width at half maximum (FWHM) bandwidth of 40 nm before being detected by the Tpx3Cam. To characterize entanglement in the polarization DoF, we measure the polarization correlation between each pair of momentum-correlated signal and idler photons. We first image the far-field of the crystal onto the Tpx3Cam using the combination of $f_1 = 50$ mm, $f_2 = 100$ mm, and $f_3 = 150$ mm lenses, and then acquire data for 16 different combinations of orientations of HWPs and QWPs, each for 1 minute. These polarization measurements allow us to reconstruct the polarization density matrices corresponding to all pairs of momentum-anticorrelated photons through quantum state tomography, which characterizes polarization entanglement. To characterize the state dimensionality in the spatial DoF, we measure the spatial correlation of signal and idler photons in the position basis. We do so by replacing the $f_3 = 150$ mm lenses with $f_3 = 75$ mm ones, thereby imaging the crystal output face (near-field) onto the Tpx3Cam sensor. We then set the HWPs and QWPs to project the

polarization in both arms into V and acquire data for 1 minute. Combined with the 16 measurements acquired in polarization characterization, the total required data acquisition time is thus $1 + 16 = 17$ minutes.

The imaging sensor in Tpx3Cam comprises a 256×256 pixel array with a pixel pitch of $55 \mu\text{m}$. The pixels in Tpx3Cam are data-driven and individually trigger the registration of photon incidence events when the signal amplitude exceeds a predefined threshold. The camera can be single-photon sensitive with the addition of an image intensifier (Photonis Cricket) and has a single photon temporal resolution of 2 ns [20]. Time-stamping for individual photons can potentially allow for more versatility in data acquisition and analysis compared to frame-based imaging devices. During data acquisition, each incident photon could hit a cluster of pixels due to being amplified by the intensifier. To correct this, we apply a centroiding algorithm that identifies the amplitude-weighted center in each cluster as the true pixel coordinate. We use the time stamp of each centroided pixel as a reference to correct the time walk within the cluster. After centroiding and time walk correction, we apply a two-pointer technique to the sorted time stamps of signal and idler photons and identify events detected within a 10-ns time window as photon coincidences [21]. Although the time walk correction

algorithm can reduce the temporal resolution to 8 ns [26, 27], it should not significantly affect the efficiency of the subsequent coincidence counting with our choice of a longer time window. As a result, we obtain an average coincidence rate of approximately 2.7 Hz between two spatially correlated 3×3 -pixel regions, which have similar sizes with the correlation widths measured at the Tpx3Cam sensor plane (see Appendix A for details). Throughout this paper, we refer to each 3×3 -pixel region as a superpixel. Moreover, we observe an overall coincidence rate of 3200 Hz between the full signal and idler fields. We note that although the experimentally measured coincidence rate is limited by the 8% overall photon detection efficiency of the Tpx3Cam system [26], our choice of 1-minute data acquisition time has allowed us to obtain enough counts for the relevant results to be statistically valid.

III. RESULTS AND DISCUSSIONS

A. Full spatial mapping of polarization entanglement

Using the setup depicted in Fig. 1(a), we perform quantum state tomography [15] using experimentally measured polarization correlation between each pair of momentum-anticorrelated (diametrically-opposite) superpixels in the far-field and reconstruct the corresponding polarization density matrix. We then compute the concurrence using $C = \max\{0, \lambda_1 - \lambda_2 - \lambda_3 - \lambda_4\}$, where λ 's are the eigenvalues of a Hermitian matrix derived from applying Pauli-y operations on reconstructed density matrices [28]. The two-photon polarization phases ϕ are computed as the phase of the $|VV\rangle\langle HH|$ elements of the reconstructed density matrices.

Fig. 2 depicts the full spatial maps of the concurrence C and two-photon polarization phase ϕ in the far field. For illustration purposes, we have mapped all signal-idler pairs to the central coordinates of the superpixels of signal photons. In Fig. 2(c), we also display a two-photon polarization density matrix, which is reconstructed at the center of the SPDC field, with the corresponding signal-idler pair indicated by a black square in Fig. 2(a-b). We calculate an average concurrence of 0.8303 ± 0.0004 , which implies strong polarization entanglement with a spatially varying structure across the entire SPDC field.

It is important to note that in Fig. 2(b), the two-photon polarization phase ϕ is highly uniform along the azimuthal direction while displaying a gradient along the radial direction, indicating highly indistinguishable polarization entanglement at each circular region concentric with the SPDC field. Consequently, if each corresponding spatial mode is also highly indistinguishable from one another, the two-photon state can be seen as being hyperentangled [14, 29], which is a tensor product of (i) spatially entangled discrete

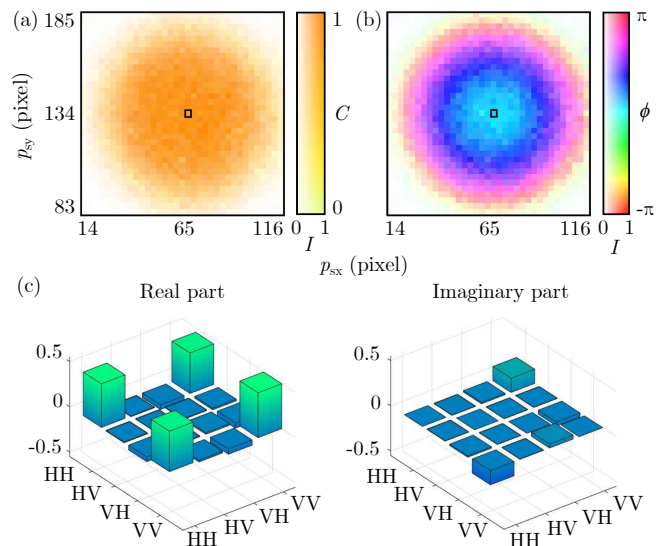


FIG. 2. (a) Concurrence C and (b) two-photon polarization phase ϕ of the two-photon states measured between momentum-correlated superpixels. The pixel coordinates correspond to the central position of the superpixels for signal photons. In the colormap, the saturation depicts the normalized pair generation rate, I , and the hue depicts C and ϕ in (a) and (b), respectively. (c) Real and imaginary parts of the density matrix reconstructed at the center of the SPDC field, the corresponding signal pixel is marked with a black square in (a) and (b).

momentum modes occupying the full spatial field of SPDC; and (ii) polarization-entangled states with a well-defined two-photon polarization phase ϕ . In the following discussions, we characterize the spatial distinguishability between all correlated spatial modes by certifying the spatial dimensionality of the two-photon state, thereby estimating an attainable total dimensionality of the full SPDC field in the joint spatial-polarization basis.

B. Certifying total attainable dimensionality of in the joint spatial-polarization bases

We characterize the spatial dimensionality of a two-photon state using its Schmidt number. While past studies have estimated this number based on certain prior assumptions about the two-photon state [30–34], some recent studies have demonstrated assumption-free protocols for certifying high dimensionality [35, 36]. In particular, it was shown that measurements in two mutually unbiased bases (MUBs) can efficiently estimate a lower bound for the Schmidt number of an entangled state, thereby certifying high-dimensional entanglement without the need for prior assumptions [35]. In our case, we show that the entanglement dimensionality in the spatial DoF can be certified by measuring the photon correlation in the discrete position basis and the discrete momentum basis, similar to the approach implemented

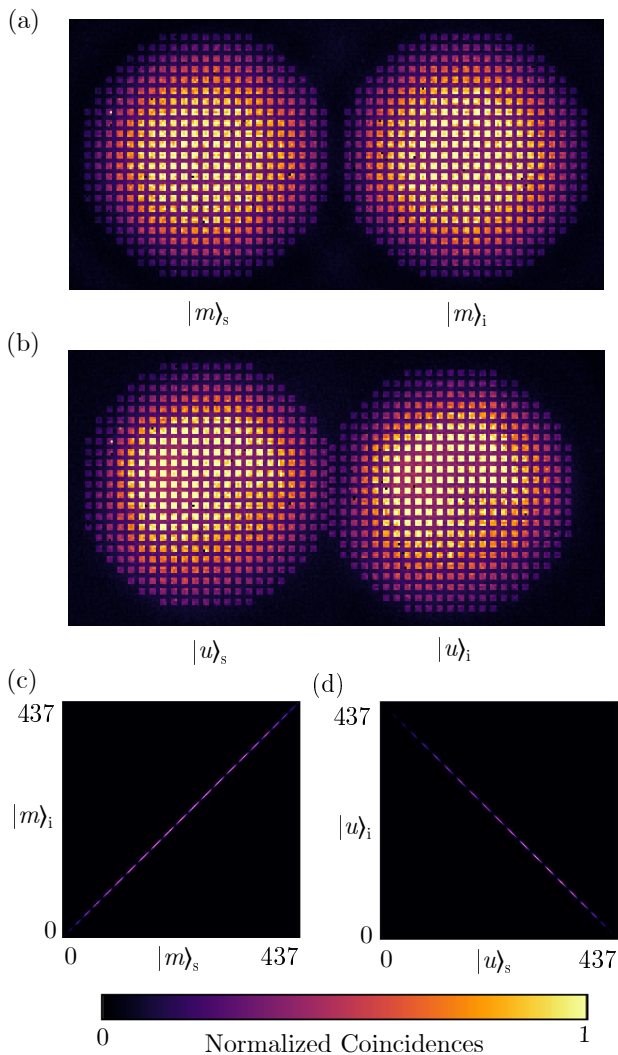


FIG. 3. Schematic depiction of (a) the discrete momentum basis in the far-field and (c) the discrete position basis in the near-field. The corresponding superpixels are depicted in a brightened color scale. Cross-correlations between the spatial modes of signal and idler photons in the (b) momentum basis and (d) position basis.

in Ref. [37].

We denote the spatial modes of the signal(idler) photons in the discrete momentum basis as $\{|m\rangle_{s(i)}\}_{m \in [1,d]}$ and in the discrete position basis as $\{|u\rangle_{s(i)}\}_{u \in [1,d]}$. Based on the experimentally measured spatial correlation widths (see Appendix B for details), individual discrete modes in the Tpx3Cam sensor plane are better approximated by 3×3 -pixel large superpixels with 2-pixel separations between adjacent superpixels. We note that since this protocol is sensitive to noise introduced by cross-talk between non-conjugate modes, a different choice in the superpixel size and separation could lead to significant underestimation of the dimensionality. As shown in Fig. 3(a-b), we select two sets of $d = 437$ superpixels evenly distributed over

the regions illuminated by signal and idler photons. The cross-correlations between spatial modes of signal and idler photons are used to calculate $\tilde{F}(\rho, \Psi)$, a lower bound for the fidelity of the experimentally measured state ρ to a maximally entangled state $|\Psi\rangle = \sum_{m=1}^d \frac{1}{\sqrt{d}} |mm\rangle$. The dimensionality of the spatial entanglement is certified to be at least $k + 1$ if k satisfies [35]

$$\tilde{F}(\rho, \Psi) > B_k(\Psi) = \sum_{m=1}^k \lambda_m^2 = \frac{k}{d}. \quad (2)$$

Upon analyzing the cross-correlations between selected spatial modes of signal and idler photons, we obtain the correlation matrices shown in Fig. 3(c-d). The fidelity lower bound is then calculated to be $\tilde{F} = 0.3383 > B_{147} = 0.3363$ (see Appendix B for details). In other words, a maximally entangled state has to have more than 147 dimensions to be transformable into our measured state through local operations and classical communication (LOCC). Therefore, the entanglement dimensionality in the spatial DoF is certified to be at least 148, indicating high indistinguishability between all correlated spatial modes.

In principle, the polarization phase ϕ in Eq. 1 can be compensated using spatial light modulators (SLMs) so that it becomes uniform also across all radial positions without reducing the polarization entanglement [7]. Consequently, we expect the attainable total dimensionality of our state to be equal to that of a global hyperentangled state, which is a product of the average dimensionality in the polarization DoF and the certified dimensionality in the spatial DoF, as underscored by the tensor product postulate of quantum physics.

Although two-photon polarization states reside in a two-dimensional Hilbert space, the effective dimensionality may be smaller for non-maximally entangled states. Therefore, it is pertinent to estimate a lower bound of the dimensionality d in the polarization DoF using the relation $\log_2 d \leq E$ [38], where E stands for the entanglement of formation [39]. For two-photon polarization states, the entanglement of formation can be derived from concurrence using [28]

$$E(C) = h\left(\frac{1 + \sqrt{1 - C^2}}{2}\right), \quad (3)$$

where $h(x) = -x \log_2 x - (1-x) \log_2 (1-x)$. The average entanglement of formation is then estimated to be $E = 0.7626 \pm 0.0003$. By multiplying the dimensionality lower bounds in spatial and polarization DoFs, we estimate the total attainable dimensionality of the entangled state to be $148 \times 2^E \approx 251$. We note that this result is likely to still be an underestimation of the actual dimensionality since the dimensionality certification protocol has limited resilience against the cross-talk noise [16, 35, 36], a more accurate estimation may be explored in a future work.

C. Native spatial-polarization coupling in SPDC processes

The spatial-polarization coupling in SPDC has two important aspects. First, the exact form of polarization entanglement depends on the transverse momenta of the *down-converted photons*. This effect, which is displayed in Fig. 2(b), occurs because down-converted photons emitted with different transverse momenta experience angle-dependent refractive indices inside the birefringent nonlinear medium and consequently accumulate different phase retardations between orthogonal polarization components. Consequently, a class of highly entangled states of the form of Eq. (1) with spatially varying ϕ is generated across the spatial profile of the field. While the spatial profile of polarization entanglement in SPDC has been studied for limited spatial regions or specific sets of spatial modes [14, 25], our results present the first full spatial distribution of polarization entanglement in the entire spatial profile of the field, laying the foundation for the controlled generation of desired photonic entangled states.

Phase-matching of the crystal also controls the relation between two-photon transverse momenta and the two-photon polarization phase. As may be noted from Fig. 2(b), the two-photon polarization phase ϕ does not vary over the full range of $-\pi$ to π in the present configuration as a consequence of the near-collinear phase matching condition. In what follows, we modify the experimental setup to show that by tuning the crystal orientation, an altered phase matching condition leads to ϕ varying over the full parameter space in the spatial profile of the field, which allows access to a much wider class of polarization-entangled states.

We depict our modified setup in Fig. 4(a). In order to capture the enlarged far-field image profile in its entirety, we deterministically split the SPDC field into two half-circles using a prism mirror (PM) and recombine the fields onto the Tpx3Cam sensor. We retain the same far-field imaging scheme, such that the two-photon correlation width remains unchanged from the earlier setup, and we again perform spatially resolved polarization state tomography using the same procedure as discussed previously. In Fig. 4(b),(c), and (d), we depict the far-field intensity Tpx3Cam image, concurrence C , and two-photon polarization phase ϕ , respectively. We again observe a strong polarization entanglement in the entire spatial extent of the field with an average concurrence of 0.8847 ± 0.0006 . We notice a marginal increase in the average concurrence compared to the result in Sec. IIIB. This is likely a result of the lower polarization cross-talk since now both signal and idler photons are detected through the transmission port of the PBS. The distribution of ϕ again displays a gradient along the radial direction, but this time with ϕ having an enlarged parameter space spanning from $-\pi$ to π . In other words, the setup produces near-maximally entangled states of Eq. (1) with all possible ϕ . Thus, our

setup can be configured to supply any specific state with a desired value of ϕ by post-selecting the corresponding pair of far-field pixels and tuning the phase-matching of the crystal. Such a mechanism can enable encoding spatial mode information in polarization correlations or vice versa, which could have important implications for quantum key distribution protocols using qudit-like states [40]. Furthermore, it is also possible to structure ϕ to have any desired profile by introducing additional phase differences between H- and V-polarized down-converted photons using SLMs to enable holographic quantum imaging [7] with much higher speed. We note that such phase structures are not limited to only manifesting in momentum space. One can observe similar effects in the near field by exploring different SPDC setup geometries. We may explore near-field phase structuring in future work.

The second important aspect of spatial-polarization structure is between the polarization DoF of the down-converted photons and the spatial DoF of the *pump beam*. Specifically, the two-photon polarization phase $\phi(\mathbf{p}_s, \mathbf{p}_i)$ in Eqn. (1) depends on the transverse momentum of the pump beam since $\mathbf{p}_p = \mathbf{p}_s + \mathbf{p}_i$ [10]. This relation is first theoretically quantified by Li et al. [10]. Here, to experimentally characterize this influence, we introduce a broader angular spectrum in the pump beam by weakly focusing it using a lens with focal length $f_0 = 100$ mm placed before the crystal. In Fig. 5, we present the influence of the angular spectrum of the pump beam on the spatial structure of the polarization states. In Fig. 5(a) and (b), we show the far-field intensity profile of the pump and the two-photon momentum correlation profile for the cases of a collimated pump and a focused pump, respectively. In Fig. 5(b), a single superpixel for the signal photons is spatially correlated with multiple superpixels for the idler photons centered around the conjugate superpixel. In other words, after focusing, the increased angular spectrum of the pump beam substantially widens the two-photon correlation width. In Fig. 5(c) and (e), we depict the results for polarization state tomography for the case of the collimated pump. To illustrate the influence of the transverse momentum of the pump beam on the polarization entanglement of the down-converted photons, we map the concurrence and phase onto pixel coordinates of the joint momentum of signal and idler, which is essentially the transverse momentum of the pump beam \mathbf{p}_p . Here, the polarization entanglement is found in a few superpixels within the narrower correlation profile, and ϕ displays little variation within the narrow angular spectrum of the collimated pump. In Fig. 5(d) and (f), we depict the results for polarization state tomography for the case of the focused pump. The concurrence map indicates the presence of polarization entanglement in all superpixels within the widened correlation profile, with an average concurrence of 0.6930 ± 0.0034 . The decrease in concurrence upon focusing the pump likely results from lower count rates and higher statistical

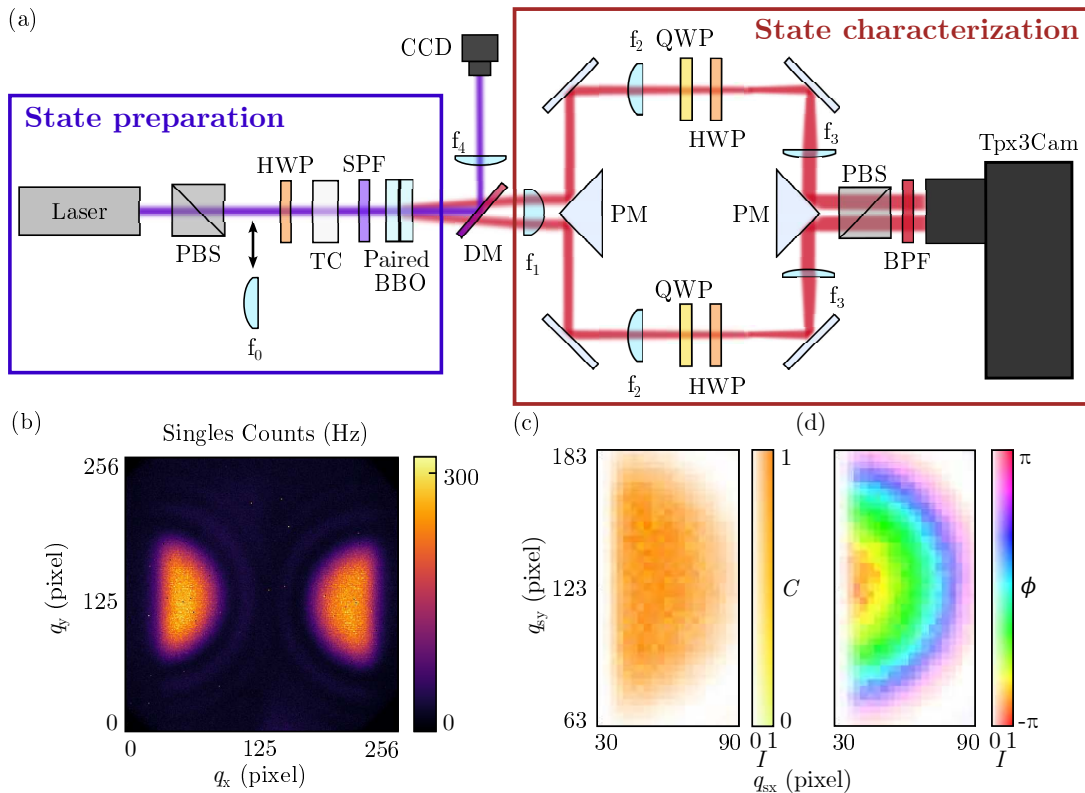


FIG. 4. (a) Schematic of the modified experimental setup. PM: prism mirror. Focal lengths of the lenses are $f_0 = 100$ mm, $f_1 = 50$ mm, $f_2 = 100$ mm, $f_3 = 150$ mm and $f_4 = 75$ mm. The angular width of the pump beam is changed by inserting f_0 into the beam path. A CCD camera images the pump beam in the Fourier plane to analyze its angular width. (b) Far-field image of the SPDC field taken by the Tpx3Cam. (c) Concurrence and (d) relative phase of the two-photon states measured between momentum-correlated superpixels. Pixel coordinates correspond to the central position of the superpixels for signal photons.

fluctuations in individual pixels. In contrast to Fig. 5(e), the phase map illustrates a gradient of ϕ dependent on the transverse momentum of the pump beam, which is in good agreement with the theoretical predictions in Fig. 2(a) of [10]. To the best of our knowledge, this is the first direct measurement of the cross-influence between the spatial DoF of the pump beam and the polarization DoF of the down-converted photons. Our work opens up the opportunity to control the spatial structure of polarization states by jointly manipulating the polarization and spatial modes of the pump, which has implications in the study of topological structures of quantum light [4, 5, 41]. For instance, one can pump a paired crystal with a beam with spatially structured polarization and directly shape the correlation between spatial mode and polarization in the nonlocal optical skyrmions[6].

IV. CONCLUSION AND OUTLOOK

In this work, we image the spatially varying polarization entanglement in a two-photon state produced from SPDC using a data-driven camera capable of time-stamping single photons. In contrast

to earlier studies that have imposed spatial-polarization structures by modulating a postselected subset of the full SPDC field, our work reveals those that are inherent to the SPDC process. By performing spatially-resolved polarization state tomography, we confirm the generation of an entire class of near-maximally polarization-entangled states with an average concurrence of 0.8303 ± 0.0004 in the entire spatial profile of the SPDC field. Additionally, we certify an attainable entanglement dimensionality of 148 in the spatial DoF using the method discussed in Refs. [35, 36], which indicates a total attainable dimensionality of 251 in the joint spatial-polarization basis. We then present the experimentally characterized spatial-polarization structure. By producing the first complete spatial map of the polarization state generated from SPDC, we illustrate the dependence of polarization entanglement on the transverse momenta of the down-converted photons in the entire spatial profile of the SPDC field. Using a weakly focused pump beam, we, for the first time, experimentally characterize the cross-influence between the polarization DoF of the down-converted photons and the spatial DoF of the pump beam. Although the current Tpx3Cam system has a low overall photon detection efficiency of 8 % [26] and

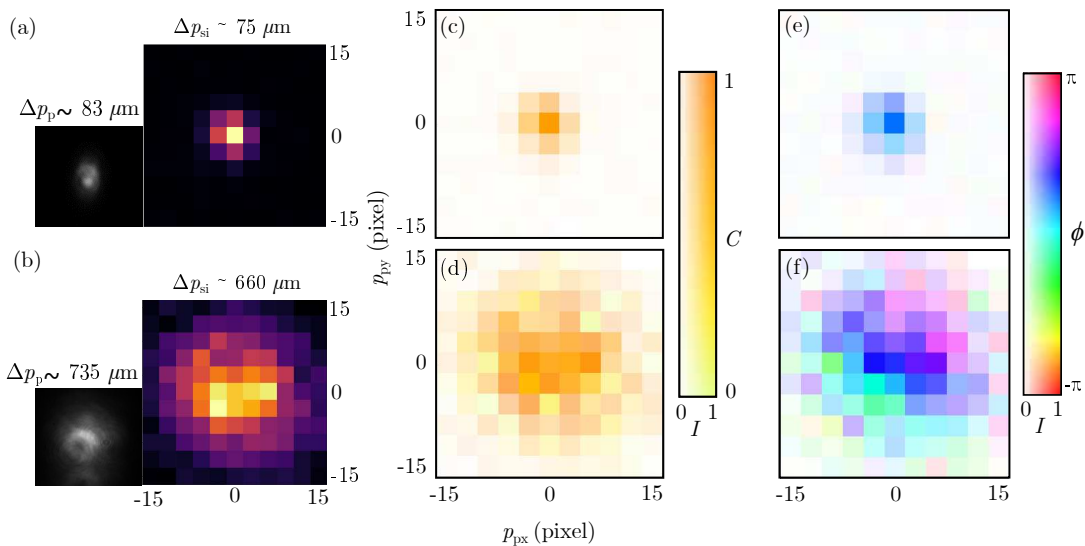


FIG. 5. Pump beam profile (greyscale image) and two-photon momentum correlation profile (colored image) for (a) collimated and (b) weakly focused pump beam. The inset captions state the beam width measured at the camera sensor plane. (c-d) Concurrence and (e-f) the two-photon polarization phase measured between a fixed signal superpixel and all momentum-correlated idler superpixels, where (c) and (e) correspond to collimated pumped beam while (d) and (f) correspond to weakly focused pump beam. Pixel coordinates indicate the transverse momenta of the pump beam $\mathbf{p}_p = \mathbf{p}_s + \mathbf{p}_i$, in which the geometrical centers of two-photon momentum correlation profile are denoted $\mathbf{p}_{px} = \mathbf{p}_{py} = 0$

is thus not yet suited for studies involving Bell-type tests of nonlocality [42], its applicability could see further expansion by implementing an image intensifier with higher quantum efficiency and higher gain. For instance, a minimum detection efficiency of 2/3 is required to close the fair-sampling loophole in Bell tests [43].

Our results could be important for future work aimed at harnessing SPDC-based entanglement generation for high-dimensional quantum information processing applications [16, 44]. For instance, time-stamping single photons with a data-driven camera could significantly reduce the acquisition time requirements in polarization entanglement-enabled holography [7], potentially enabling fast super-resolution imaging and microscopy [45]. Our results on cross-influence between different DoFs could extend the recent demonstration of hiding images in quantum correlations [12] to hiding and rapidly reconstructing complex phase images in spatial and polarization correlations. On the fundamental side, our work can be extended to explore the spatial-polarization coupling in different entanglement generation schemes. For instance, it is possible to spatially resolve the polarization entanglement produced from post-selecting down-converted photons from a single Type-II nonlinear crystal [11, 46], thereby further deepening our understanding of the cross-DoF coupling in SPDC. Furthermore, our work could have important implications for studying and engineering hyperentangled photon states for various applications, such as noise-resilient quantum illumination [47], quantum key distribution with high secure key rates [48–50]. It may also be possible to build on existing work on exchange

phases in Hong-Ou-Mandel interference involving high-dimensional hyperentangled photons [51] and spatially resolve such effects for a hyperentangled state.

ACKNOWLEDGMENTS

The authors thank X. Gao, A. D’Errico, B. Braverman, S. Karan, and M. Krenn for fruitful discussions. C. L. acknowledges P. Svihra for helpful advice on data processing. The portion of the work performed at the University of Ottawa was supported by the Canada Research Chairs program under Award 950-231657, the Natural Sciences and Engineering Research Council of Canada under Alliance Consortia Quantum Grant ALLRP 578468 - 22, Discovery Grant RGPIN/2017-06880, and the Canada First Research Excellence Fund Award 072623. In addition, R.W.B. acknowledges support through U.S. National Science Foundation Award No. 2138174 and U.S. Department of Energy Award No. FWP 76295.

Appendix A: Observation of spatial entanglement through the violation of Einstein-Podolsky-Rosen criteria

In Fig. 6, we depict the experimentally measured x - and y -components of the spatial correlation profile in both the position and momentum basis. We note the strong position correlations and momentum anti-correlations between the photons, which is

a characteristic feature of spatial entanglement. Specifically, Fig. 6(c) and (f) depict the biphoton correlation profiles in the joint momentum and position coordinates of the down-converted photons. From these results, we conclude that in the Tpx3Cam sensor plane, individual discrete momentum and position modes are best approximated by 3×3 -pixel large superpixels.

The results also allow us to quantitatively verify spatial entanglement by demonstrating violations of the Einstein-Podolsky-Rosen (EPR) criteria [52, 53]. We first obtain near-field (NF) and far-field (FF) correlation widths Δ_{NF} and Δ_{FF} , respectively, at the Tpx3Cam sensor plane by fitting Gaussians to the spatial correlation profiles of Fig. 6 in the x - and y -directions [30, 53, 54]. We then calculate the position and momentum uncertainties using the relations

$$\Delta(p_{ir}|p_{sr}) = \frac{k_{si}\hbar}{f_e}\Delta_{\text{FF}}, \quad (\text{A1a})$$

$$\Delta(q_{ir}|q_{sr}) = \frac{1}{M}\Delta_{\text{NF}}, \quad (\text{A1b})$$

where $p_{sr(ir)}$ and $q_{sr(ir)}$ stand for the momentum and position of the signal (idler) photons, respectively, $r = x, y$ represent the x - and y -components of the quantities, $k_{si} = (2\pi/810) \text{ nm}^{-1}$ is the wavevector of the signal and idler photons, $f_e = 75 \text{ mm}$ is the effective focal length of our far-field imaging system and $M = 2$ is the magnification of our near-field imaging system. We summarize our results in Table 1 and compute the conditional Heisenberg uncertainty products as

$$\Delta_{\min}p_x\Delta_{\min}q_x = (0.11 \pm 0.05)\hbar < \hbar/2, \quad (\text{A2a})$$

$$\Delta_{\min}p_y\Delta_{\min}q_y = (0.12 \pm 0.03)\hbar < \hbar/2, \quad (\text{A2b})$$

which clearly violates the EPR criteria in both the x - and y -directions. We note that the asymmetry observed in the x -components of the position correlation, which is depicted in Fig. 6(d), is likely a consequence of a distortion in the pump's intensity profile. As depicted in Fig. 1(c) in the main text, the near-field singles rates display a non-Gaussian spatial profile as a result of the distorted pump profile. Although this imperfection may affect the verification of spatial entanglement using the EPR criterion, which requires the pump beam to have a Gaussian profile [30], it does not refute our conclusions regarding the certification of hyperentanglement, as our entanglement certification protocol does not rely on Gaussian approximations of the SPDC field profiles [36].

Appendix B: Estimation of fidelity lower bound

Following the approaches described in [37], we certify the dimensionality of entanglement in the spatial degree of freedom using correlations in two mutually unbiased

TABLE I. Measurement uncertainties inferred from spatial correlation profiles

Quantity	Values	Units
$\Delta_{\min}p_x$	$(4.9 \pm 0.2) \times 10^{-3}$	$\hbar/\mu\text{m}$
$\Delta_{\min}p_y$	$(6.4 \pm 0.3) \times 10^{-3}$	$\hbar/\mu\text{m}$
$\Delta_{\min}q_x$	18.76 ± 9.49	μm
$\Delta_{\min}q_y$	18.18 ± 3.63	μm

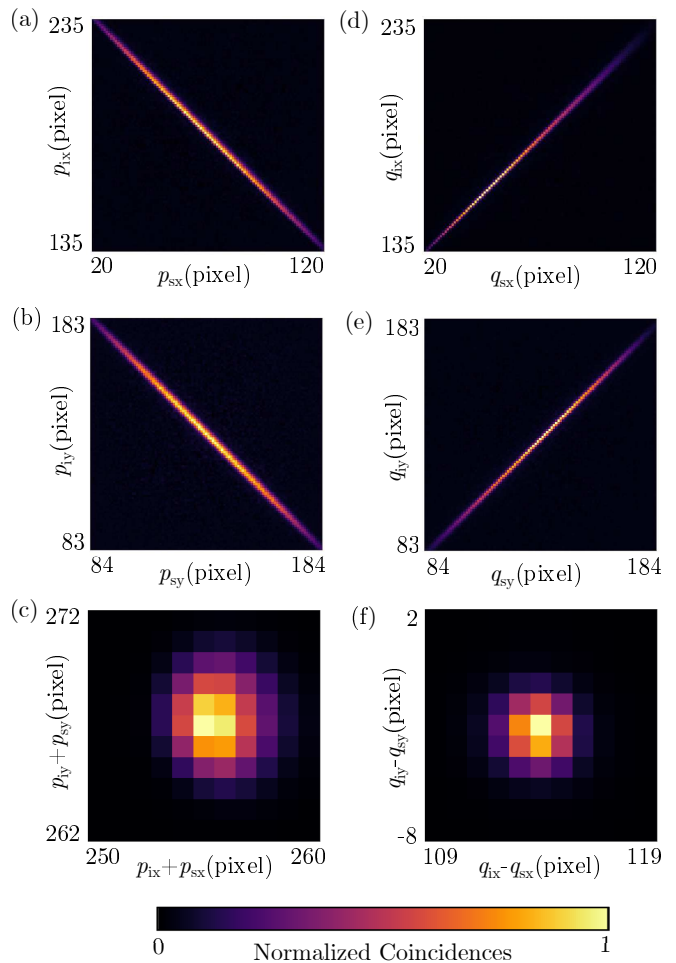


FIG. 6. Spatial correlation profiles measured in the x -components, y -components, and joint coordinates of the (a-c) momentum and (d-f) position of the signal-idler photons.

bases (MUBs) [35, 36]. In the main text, we have defined the two MUBs to be the discrete momentum basis $\{|m\rangle_{s(i)}\}_{m \in [1,d]}$ and the discrete position basis $\{|u\rangle_{s(i)}\}_{u \in [1,d]}$.

The fidelity $F(\rho, \Psi)$ of the experimentally measured state ρ to a maximally entangled state $|\Psi\rangle = \sum_{m=1}^d \frac{1}{\sqrt{d}} |mm\rangle$ is defined as:

$$\begin{aligned}
F(\rho, \Psi) &= \text{Tr}(|\Psi\rangle\langle\Psi|\rho) \\
&= \sum_{m,n=1}^d \langle mm|\rho|nn\rangle \\
&= F_1(\rho, \Psi) + F_2(\rho, \Psi),
\end{aligned} \tag{B1}$$

where

$$F_1(\rho, \Psi) = \frac{1}{d} \sum_{m=1}^d \langle mm|\rho|mm\rangle, \tag{B2}$$

$$F_2(\rho, \Psi) = \frac{1}{d} \sum_{m \neq n} \langle mm|\rho|nn\rangle. \tag{B3}$$

Since for an arbitrary state ρ with a Schmidt number

of $k \leq d$, the fidelity satisfies

$$F(\rho, \Psi) \leq B_k(\Psi) = \frac{k}{d}, \tag{B4}$$

the entanglement dimensionality of a state with $F(\rho, \Psi) > B_k(\Psi)$ must be at least $k + 1$. As we will show in the following, correlations in the two MUBs will allow us to obtain a lower bound for the fidelity via $\tilde{F}(\rho, \Psi) = F_1(\rho, \Psi) + \tilde{F}_2(\rho, \Psi) \leq F_1(\rho, \Psi) + F_2(\rho, \Psi) = F(\rho, \Psi)$

The coincidence counts N_{mn} measured in the discrete momentum basis allow us to calculate $F_1(\rho, \Psi)$ using

$$\langle mn|\rho|mn\rangle = \frac{N_{mn}}{\sum_{k,l} N_{kl}}. \tag{B5}$$

Supplementing the coincidence counts N_{uv} measured in the discrete position basis allows us to calculate $\tilde{F}_2(\rho, \Psi)$, the lower bound of $F_2(\rho, \Psi)$, via

$$\tilde{F}_2(\rho, \Psi) = \sum_{u=0}^{d-1} \langle uu|\rho|uu\rangle - \frac{1}{d} - \sum_{m \neq n', m' \neq n, n \neq n', n' \neq m'} \gamma_{mnm'n'} \sqrt{\langle mn|\rho|mn\rangle \langle m'n'|\rho|m'n'\rangle}, \tag{B6}$$

where

$$\langle uv|\rho|uv\rangle = \frac{N_{uv}}{\sum_{k,l} N_{kl}}, \tag{B7}$$

$$\gamma_{mnm'n'} = \begin{cases} 0 & \text{if } (m - m' - n + n') \bmod d \neq 0 \\ 1/d & \text{otherwise.} \end{cases} \tag{B8}$$

-
- [1] S. E. Harris, M. K. Oshman, and R. L. Byer, Observation of tunable optical parametric fluorescence, *Phys. Rev. Lett.* **18**, 732 (1967).
- [2] D. C. Burnham and D. L. Weinberg, Observation of simultaneity in parametric production of optical photon pairs, *Physical Review Letters* **25**, 84 (1970), publisher: American Physical Society.
- [3] Y. H. Shih and C. O. Alley, New type of Einstein-Podolsky-Rosen-Bohm experiment using pairs of light quanta produced by optical parametric down conversion, *Phys. Rev. Lett.* **61**, 2921 (1988).
- [4] C. He, Y. Shen, and A. Forbes, Towards higher-dimensional structured light, *Light: Science & Applications* **11**, 205 (2022), number: 1 Publisher: Nature Publishing Group.
- [5] I. Nape, B. Sephton, P. Ornelas, C. Moodley, and A. Forbes, Quantum structured light in high dimensions, *APL Photonics* **8**, 051101 (2023).
- [6] P. Ornelas, I. Nape, R. de Mello Koch, and A. Forbes, Non-local skyrmions as topologically resilient quantum entangled states of light, *Nature Photonics* **18**, 258 (2024).
- [7] H. Defienne, B. Ndagano, A. Lyons, and D. Faccio, Polarization entanglement-enabled quantum holography, *Nature Physics* **17**, 591 (2021), number: 5 Publisher: Nature Publishing Group.
- [8] G. Vallone, G. Donati, R. Ceccarelli, and P. Mataloni, Six-qubit two-photon hyperentangled cluster states: Characterization and application to quantum computation, *Phys. Rev. A* **81**, 052301 (2010).
- [9] M. Ciampini, A. Orioux, S. Paesani, *et al.*, Path-polarization hyperentangled and cluster states of photons on a chip, *Light: Science & Applications* **5**, e16064 (2016).
- [10] C. Li, B. Braverman, G. Kulkarni, and R. W. Boyd, Experimental generation of polarization entanglement from spontaneous parametric down-conversion pumped by spatiotemporally highly incoherent light,

- Physical Review A **107**, L041701 (2023), publisher: American Physical Society.
- [11] W. Zhang, D. Xu, and L. Chen, Polarization entanglement from parametric down-conversion with an LED pump, *Physical Review Applied* **19**, 054079 (2023), publisher: American Physical Society.
- [12] C. Vernière and H. Defienne, Hiding images in quantum correlations, *Phys. Rev. Lett.* **133**, 093601 (2024).
- [13] P. G. Kwiat, E. Waks, A. G. White, I. Appelbaum, and P. H. Eberhard, Ultrabright source of polarization-entangled photons, *Physical Review A* **60**, R773 (1999), publisher: American Physical Society.
- [14] J. T. Barreiro, N. K. Langford, N. A. Peters, and P. G. Kwiat, Generation of hyperentangled photon pairs, *Physical Review Letters* **95**, 260501 (2005), publisher: American Physical Society.
- [15] D. F. V. James, P. G. Kwiat, W. J. Munro, and A. G. White, Measurement of qubits, *Physical Review A* **64**, 052312 (2001), publisher: American Physical Society.
- [16] N. Friis, G. Vitagliano, M. Malik, and M. Huber, Entanglement certification from theory to experiment, *Nature Reviews Physics* **1**, 72 (2019), number: 1 Publisher: Nature Publishing Group.
- [17] N. Herrera Valencia, V. Srivastav, M. Pivoluska, M. Huber, N. Friis, W. McCutcheon, and M. Malik, High-Dimensional Pixel Entanglement: Efficient Generation and Certification, *Quantum* **4**, 376 (2020).
- [18] M. Fisher-Levine and A. Nomerotski, Timepixcam: a fast optical imager with time-stamping, *Journal of Instrumentation* **11** (03), C03016.
- [19] A. Nomerotski, Imaging and time stamping of photons with nanosecond resolution in timepix based optical cameras, *Nuclear Instruments and Methods in Physics Research Section A: Accelerators, High Energy Physics, Detectors and Associated Equipment* **904**, 162501 (2018), publisher: Elsevier.
- [20] A. Nomerotski, M. Chekhlov, D. Dolzhenko, R. Glazenberg, B. Farella, M. Keach, R. Mahon, D. Orlov, and P. Svihra, Intensified tpx3cam, a fast data-driven optical camera with nanosecond timing resolution for single photon detection in quantum applications, *Journal of Instrumentation* **18** (01), C01023.
- [21] C. Ianzano, P. Svihra, M. Flament, A. Hardy, G. Cui, A. Nomerotski, and E. Figueroa, Fast camera spatial characterization of photonic polarization entanglement, *Scientific Reports* **10**, 6181 (2020), number: 1 Publisher: Nature Publishing Group.
- [22] B. Courme, C. Vernière, P. Svihra, S. Gigan, A. Nomerotski, and H. Defienne, Quantifying high-dimensional spatial entanglement with a single-photon-sensitive time-stamping camera, *Optics Letters* **48**, 3439 (2023), publisher: Optica Publishing Group.
- [23] X. Gao, Y. Zhang, A. D'Errico, A. Sit, K. Heshami, and E. Karimi, Full spatial characterization of entangled structured photons, *Phys. Rev. Lett.* **132**, 063802 (2024).
- [24] Y. Nambu, K. Usami, Y. Tsuda, K. Matsumoto, and K. Nakamura, Generation of polarization-entangled photon pairs in a cascade of two type-i crystals pumped by femtosecond pulses, *Physical Review A* **66**, 033816 (2002), publisher: American Physical Society.
- [25] J. B. Altepeter, E. R. Jeffrey, and P. G. Kwiat, Phase-compensated ultra-bright source of entangled photons, *Optics Express* **13**, 8951 (2005), publisher: Optica Publishing Group.
- [26] V. Vidyapin, Y. Zhang, D. England, and B. Sussman, Characterisation of a single photon event camera for quantum imaging, *Scientific Reports* **13**, 1009 (2023).
- [27] Y. Zhang, D. England, A. Nomerotski, P. Svihra, S. Ferrante, P. Hockett, and B. Sussman, Multidimensional quantum-enhanced target detection via spectrotemporal-correlation measurements, *Phys. Rev. A* **101**, 053808 (2020).
- [28] W. K. Wootters, Entanglement of formation of an arbitrary state of two qubits, *Physical Review Letters* **80**, 2245 (1998), publisher: American Physical Society.
- [29] P. G. Kwiat, Hyper-entangled states, *Journal of Modern Optics* **44**, 2173 (1997).
- [30] C. K. Law and J. H. Eberly, Analysis and interpretation of high transverse entanglement in optical parametric down conversion, *Physical Review Letters* **92**, 127903 (2004), publisher: American Physical Society.
- [31] H. Di Lorenzo Pires, C. H. Monken, and M. P. van Exter, Direct measurement of transverse-mode entanglement in two-photon states, *Phys. Rev. A* **80**, 022307 (2009).
- [32] M. P. Edgar, D. S. Tasca, F. Izdebski, R. E. Warburton, J. Leach, M. Agnew, G. S. Buller, R. W. Boyd, and M. J. Padgett, Imaging high-dimensional spatial entanglement with a camera, *Nature Communications* **3**, 984 (2012), number: 1 Publisher: Nature Publishing Group.
- [33] F. Devaux, A. Mosset, P.-A. Moreau, and E. Lantz, Imaging spatiotemporal hong-ou-mandel interference of biphoton states of extremely high schmidt number, *Phys. Rev. X* **10**, 031031 (2020).
- [34] X. Gao, Y. Zhang, A. D'Errico, K. Heshami, and E. Karimi, High-dimensional detection of spatial correlations in hong-ou-mandel interference, *Opt. Express* **30**, 19456 (2022).
- [35] J. Bavaresco, N. Herrera Valencia, C. Klöckl, M. Pivoluska, P. Erker, N. Friis, M. Malik, and M. Huber, Measurements in two bases are sufficient for certifying high-dimensional entanglement, *Nature Physics* **14**, 1032 (2018), number: 10 Publisher: Nature Publishing Group.
- [36] P. Erker, M. Krenn, and M. Huber, Quantifying high dimensional entanglement with two mutually unbiased bases, *Quantum* **1**, 22 (2017), publisher: Verein zur Förderung des Open Access Publizierens in den Quantenwissenschaften.
- [37] B. Ndagano, H. Defienne, A. Lyons, I. Starshynov, F. Villa, S. Tisa, and D. Faccio, Imaging and certifying high-dimensional entanglement with a single-photon avalanche diode camera, *npj Quantum Information* **6**, 1 (2020), number: 1 Publisher: Nature Publishing Group.
- [38] M. A. Nielsen and I. L. Chuang, *Quantum Computation and Quantum Information: 10th Anniversary Edition* (Cambridge University Press, 2010).
- [39] W. K. Wootters, Entanglement of formation and concurrence, *Quantum Info. Comput.* **1**, 27–44 (2001).
- [40] L. Scarfe, R. Abolhassani, F. Bouchard, A. Z. Goldberg, K. Heshami, F. Di Colandrea, and E. Karimi, High-dimensional quantum key distribution with qubit-like states, *Communications Physics* **8**, 472 (2025).

- [41] Y. Shen, Q. Zhang, P. Shi, L. Du, X. Yuan, and A. V. Zayats, Optical skyrmions and other topological quasiparticles of light, *Nature Photonics* **18**, 15 (2024).
- [42] C. K. Zeitler, J. C. Chapman, E. Chitambar, and P. G. Kwiat, Entanglement verification of hyperentangled photon pairs, *Phys. Rev. Appl.* **18**, 054025 (2022).
- [43] N. Gisin and B. Gisin, A local hidden variable model of quantum correlation exploiting the detection loophole, *Physics Letters A* **260**, 323 (1999).
- [44] M. Erhard, M. Krenn, and A. Zeilinger, Advances in high-dimensional quantum entanglement, *Nature Reviews Physics* **2**, 365 (2020), number: 7 Publisher: Nature Publishing Group.
- [45] H. Defienne, P. Cameron, B. Ndagano, A. Lyons, M. Reichert, J. Zhao, A. R. Harvey, E. Charbon, J. W. Fleischer, and D. Faccio, Pixel super-resolution with spatially entangled photons, *Nature Communications* **13**, 3566 (2022).
- [46] C. E. Kuklewicz, M. Fiorentino, G. Messin, F. N. C. Wong, and J. H. Shapiro, High-flux source of polarization-entangled photons from a periodically poled KTiO_4 parametric down-converter, *Phys. Rev. A* **69**, 013807 (2004).
- [47] A. V. Prabhu, B. Suri, and C. M. Chandrashekar, Hyperentanglement-enhanced quantum illumination, *Phys. Rev. A* **103**, 052608 (2021).
- [48] F. Wu, G. Yang, H. Wang, J. Xiong, F. Alzahrani, A. Hobiny, and F. Deng, High-capacity quantum secure direct communication with two-photon six-qubit hyperentangled states, *Science China Physics, Mechanics & Astronomy* **60**, 120313 (2017).
- [49] J.-H. Kim, Y. Kim, D.-G. Im, C.-H. Lee, J.-W. Chae, G. Scarcelli, and Y.-H. Kim, Noise-resistant quantum communications using hyperentanglement, *Optica* **8**, 1524 (2021).
- [50] L. Nemirovsky-Levy, U. Pereg, and M. Segev, Increasing quantum communication rates using hyperentangled photonic states, *Optica Quantum* **2**, 165 (2024).
- [51] Z.-F. Liu, C. Chen, J.-M. Xu, Z.-M. Cheng, Z.-C. Ren, B.-W. Dong, Y.-C. Lou, Y.-X. Yang, S.-T. Xue, Z.-H. Liu, W.-Z. Zhu, X.-L. Wang, and H.-T. Wang, Hong-ou-mandel interference between two hyperentangled photons enables observation of symmetric and antisymmetric particle exchange phases, *Phys. Rev. Lett.* **129**, 263602 (2022).
- [52] M. D. Reid, Demonstration of the einstein-podolsky-rosen paradox using nondegenerate parametric amplification, *Physical Review A* **40**, 913 (1989), publisher: American Physical Society.
- [53] A. Bhattacharjee, N. Meher, and A. K. Jha, Measurement of two-photon position-momentum einstein-podolsky-rosen correlations through single-photon intensity measurements, *New Journal of Physics* **24**, 053033 (2022).
- [54] C. H. Monken, P. H. S. Ribeiro, and S. Pádua, Transfer of angular spectrum and image formation in spontaneous parametric down-conversion, *Physical Review A* **57**, 3123 (1998), publisher: American Physical Society.